coatings

MDPI

Article

Predicting the Residual Stress of Amorphous Al_2O_3-Y_2O_3 Nano-Laminated Deuterium Permeation Barrier under Thermal Cycles

Kezhi Huang [1,2,3,†], Hao Liu [1,2,4,†], Weijing Wang [1,2,3], Qinghe Yu [1,2,3,4,*], Liwu Jiang [5], Yu Liu [1,2,4], Jing Mi [1,2,*], Lei Hao [1,2,3,*], Baolong Yuan [1,2,*], Mingkun Liu [2,*], Rui Cai [6,*] and Wei Xiao [2]

1 National Engineering Research Center of Nonferrous Metals Materials and Products for New Energy, GRINM Group Co., Ltd., Beijing 100088, China
2 GRIMAT Engineering Institute Co., Ltd., Beijing 101407, China
3 General Research Institute for Nonferrous Metals, Beijing 100088, China
4 GRINM (GuangDong) Institute for Advanced Materials and Technology, Shenzhen 518055, China
5 National Center for Materials Service Safety, University of Science and Technology Beijing, Beijing 100083, China
6 State Key Laboratory for Performance and Structure Safety of Petroleum Tubular Goods and Equipment Materials, CNPC Tubular Goods Research Institute, Xi'an 710077, China
* Correspondence: yuqh@grinm.com (Q.Y.); mijing@grinm.com (J.M.); haolei@grinm.com (L.H.); yuanbl@grinm.com (B.Y.); liumingkun@grinm.com (M.L.); cair@cnpc.com.cn (R.C.)
† These authors contributed equally to this work.

Abstract: Al_2O_3-Y_2O_3 laminated coating can be applied in fusion reactors to prevent fuel leakage and radiological hazard. However, the residual stress induced by the thermal cycles during the operation of the reactor can cause the failure of the coating. In order to analyze the problem, finite element models of Al_2O_3-Y_2O_3 laminated coatings with 600 nm of total thickness and different layout were analyzed. The max principal stress site in the coatings is located at the sub-top layer. The max principal stress in laminated coating with the Y_2O_3 sub-top decreases from 657 MPa for a two-layer coating (300 nm) to 598 MPa for a four-layer coating (150 nm). On the contrary, if Al_2O_3 is the sub-top layer, the max principal stress increases from 463 MPa for a two-layer coating (300 nm) to 495 MPa for a four-layer coating (150 nm). The result shows that the more deformable amorphous Al_2O_3 layer in the laminated coating system is more influential to the thermal stress.

Keywords: deuterium permeation barrier; finite element analysis; laminated coating; thermal stress

Citation: Huang, K.; Liu, H.; Wang, W.; Yu, Q.; Jiang, L.; Liu, Y.; Mi, J.; Hao, L.; Yuan, B.; Liu, M.; et al. Predicting the Residual Stress of Amorphous Al_2O_3-Y_2O_3 Nano-Laminated Deuterium Permeation Barrier under Thermal Cycles. *Coatings* **2022**, *12*, 1780. https://doi.org/10.3390/coatings12111780

Academic Editor: Alessandro Latini

Received: 24 October 2022
Accepted: 13 November 2022
Published: 21 November 2022

1. Introduction

Fusion energy has become attractive as a clean energy source to solve future energy issues [1,2]. However, tritium, the fuel of the fusion reactor, is radioactive and can easily permeate through structural materials such as 316L stainless steel, resulting in fuel leakages and hydrogen embrittlement of the structure, and thus threatening the safe operation of the fusion reactor [2,3]. In the tritium cycles of fusion reactor as shown in Figure 1, tritium loss is mainly due to its leakage into the coolant and forming tritiated water (HTO) then exhausted to the outside environment [2,4].

Hanchar and Kazim analyzed the tritium leakage of *starfire*-Interim tokamak reactor and obtained a stunning result that the tritium losses in the primary coolant loop exceed 10^3 Ci/day, obviously unacceptable by any standard [4]. The HTO molecule can easily be incorporated into the human body, where it has a half residual life of 10 days according to ICRP Publication 71 [5]. Tritium permeation is dangerous and must be prevented. Currently, the most used solution to this critical problem is preparing a ceramic coating on the structural steel. Because tritium is strictly controlled, deuterium and hydrogen are commonly used as substitutes to analyze the performance of coatings in experiments.

Oxide ceramics such as Al_2O_3, Cr_2O_3, Y_2O_3, Er_2O_3, TiO_2 and their composites are the most common choice because they can effectively suppress the deuterium permeation and their cost is acceptable [6–13]. Among them, Al_2O_3 has a high permeation resistant factor (PRF), high strength, strong thermodynamic stability, and relatively low cost and easy deposition method. Thus, Al_2O_3 is an ideal candidate for preparing a deuterium permeation barrier. Al_2O_3 has been applied in fusion industry acting as highly radiation-resistant material for optical and dielectric windows [14,15]. However, the vast thermal mismatch between the Al_2O_3 coating and the substrate, 316L stainless steel, e.g., can cause huge residual stress in the system, resulting in the peeling-off of the coating [16–19]. Many studies have been conducted to analyze the residual thermal stress and failure behavior of the coating/substrate system in order to determine the failure mechanism and the optimization procedures. Preparing multiple-layer coating or gradient coating is the most widely used solution to the thermal mismatch problem currently [20–28]. Some researchers found that cracks and defects in the coating could produce a significant effect on the fracture of the coating. Low density micro crack will dramatically degrade the coating [29,30]. However, most of them focus on monolayer or bilayer micron-thick coatings. Resent findings showed that nano-thick coatings have better performance than micron ones [31,32]. Furthermore, our previous findings [33] indicates that the interface between layers in a bilayer Al_2O_3/Y_2O_3 coating if not introducing much defects can act as a barrier that blocks the permeation of tritium. Thus, the composite coating has a higher permeation resistance than the single layer ones. To explore the effect of introducing multiple interfaces in a nano-thick laminated coating on the thermal cycle behavior of the coating, the residual thermal stress in Al_2O_3-Y_2O_3 laminated coatings was investigated via finite element analysis. The effect of the layer thickness, coating lay-out, and temperature difference on the residual thermal stress of Al_2O_3-Y_2O_3 laminated coating were analyzed. This research is a preliminary work for understanding the thermal cycle behavior of a nano-thick laminated deuterium permeation barrier and the optimization of the preparation of such coating.

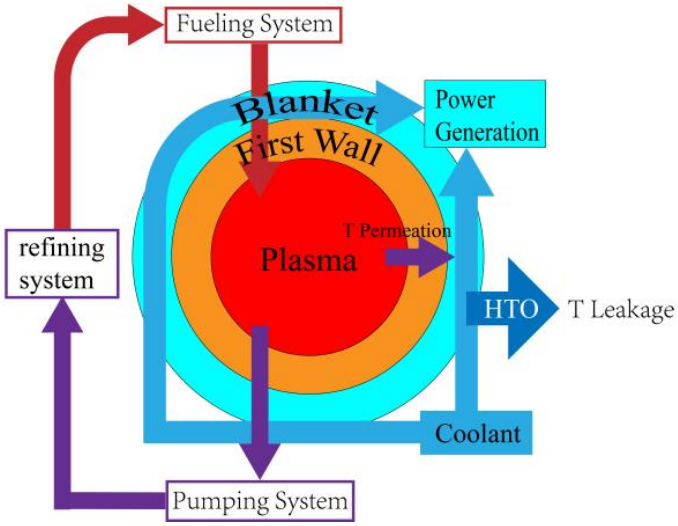

Figure 1. Tritium cycle and leakage in fusion reactor [2,4].

2. Materials and Methods

Static structural analysis via ANSYS 19 was used to simulate the thermal stress of the coating/substrate systems under thermal cycles. Max principal stress was selected as the major evaluation factor, because oxide ceramics are brittle and sensitive to b tensile stress.

2.1. Analytic Model

The finite-element analysis model settings are similar to our previous work on bilayer Al_2O_3/Y_2O_3 and Y_2O_3/Al_2O_3 coatings [33]. Static structural finite-element analysis was applied and displacements are defined as solution factors corresponding to each nodal element. Loads are derived from forces and displacements. The finite-element analysis software uses interpolation functions to figure out the elemental stiffness matrix to calculate the stress and strain increments at any point in the model.

The total strain vector, $\{\Delta\varepsilon\}$, is the sum of elastic strain increment vector, $\left\{\Delta\varepsilon^{el}\right\}$, and thermal strain increment vector, $\left\{\Delta\varepsilon^{th}\right\}$:

$$\{\Delta\varepsilon\} = \left\{\Delta\varepsilon^{el}\right\} + \left\{\Delta\varepsilon^{th}\right\}. \quad (1)$$

Within each element, the displacement, $\{\delta\}$, for any given element, (e) can be calculated using following equation:

$$\{\Delta\varepsilon\} = \{B\}\{\delta\}^e, \quad (2)$$

where $\{B\}$ is the strain matrix.

Hooke's law can be applied to figure out the elastic stress increment vector, $\left\{\Delta\sigma^{el}\right\}$:

$$\left\{\Delta\sigma^{el}\right\} = \{D\}\left\{\Delta\varepsilon^{el}\right\}, \quad (3)$$

where $\{D\}$ is the elastic matrix for any given material that defined by its elastic modulus, E, and Poisson's ratio, ν, at a given temperature.

The relationship between the thermal stress increment vector, $\left\{\Delta\varepsilon^{th}\right\}$, and the temperature increment, ΔT, can be calculated as follows:

$$\left\{\Delta\varepsilon^{th}\right\} = \{\alpha\}\Delta T, \quad (4)$$

where α is the thermal expansion coefficient.

The principle of virtual work is applied to figure out the stress:

$$\{\delta\}^T\{\Delta F\}^e = \int\int\int \{\varepsilon\}^T\{\sigma\}dxdydz. \quad (5)$$

Substitution of Equations (3)–(5) derives:

$$\{\Delta F\}^e = \int\int\int \{B\}^T\{D\}\{\Delta\varepsilon^e\}dxdydz. \quad (6)$$

The equilibrium equation can be applied to calculate the element stiffness matrix, $\{K\}$:

$$\{K\}\{\delta\} = \{F\} \quad (7)$$

The load vector $\{\Delta F\}$. only includes the thermal force in the thermal shock condition, Thus, the thermal stress can be derived as follows:

$$\{\Delta F\}_T^e = \int\int\int \{B\}^T\{D\}\{B\}\{\alpha\}dxdydz. \quad (8)$$

2.2. Model Geometry and Material Properties

The modeling was based on the composite coatings in our previous study [25]. The scanning electron microscope (SEM) (Hitachi-S4800, Hitachi, Tokyo, Japan) images of the coatings deposited on 316L stainless steel by radio-frequency magnetron sputtering are shown in Figure 2. As the figure shows, the interface between each layer is considerably smooth and clear with no visible defects. It indicates that each layer of the coating is dense

and homogeneous. Further description about the deposition and the performance of the coatings can be found in [32].

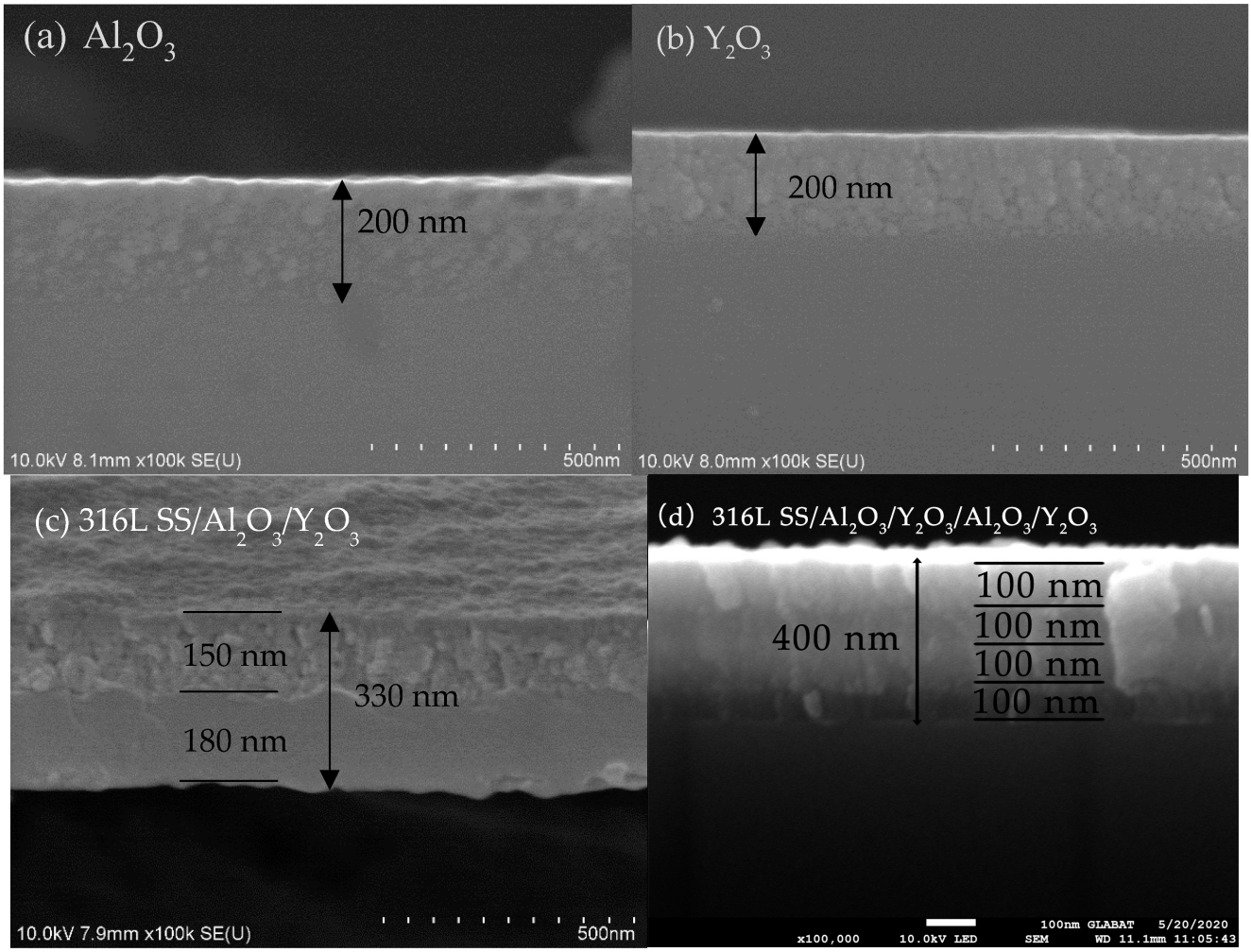

Figure 2. SEM images of the nanoscale coatings: (**a**) Al_2O_3 [32]; (**b**) Y_2O_3 [34]; (**c**) 316L SS/Al_2O_3/Y_2O_3 [32]; (**d**) 316L SS/Al_2O_3/Y_2O_3/Al_2O_3/Y_2O_3.

The model consists of two major parts. One was the substrate modeled as a cylinder which was 1 mm in diameter and 0.5 mm in thickness. The other is the laminated coating, where the thickness of each layer is t_i, i is the order of the layer from substrate to the top, and t_0 is the thickness of the substrate. Laminated coatings with different deposition orders were analyzed. The model configuration is shown in Table 1.

Table 1. Model configuration.

Structure Series	Number	Structure	Total Thickness (nm)	Layer Thickness (nm)
Series 1	1	316L/Al_2O_3/Y_2O_3	600	300
(laminated coatings	2	316L/Y_2O_3/Al_2O_3/Y_2O_3	600	200
with Y_2O_3 top coat)	3	316L/Al_2O_3/Y_2O_3/Al_2O_3/Y_2O_3	600	150
Series 2	6	316L/Y_2O_3/Al_2O_3	600	300
(laminated coatings	7	316L/Al_2O_3/Y_2O_3/Al_2O_3	600	200
with Al_2O_3 top coat)	8	316L/Y_2O_3/Al_2O_3/Y_2O_3/Al_2O_3	600	150

Each layer is uniform and homogenous. Thus, it is possible and proper to use two-dimensional axisymmetric models to simplify the analysis, as shown in Figure 3. The properties of the materials involved are listed in Table 2.

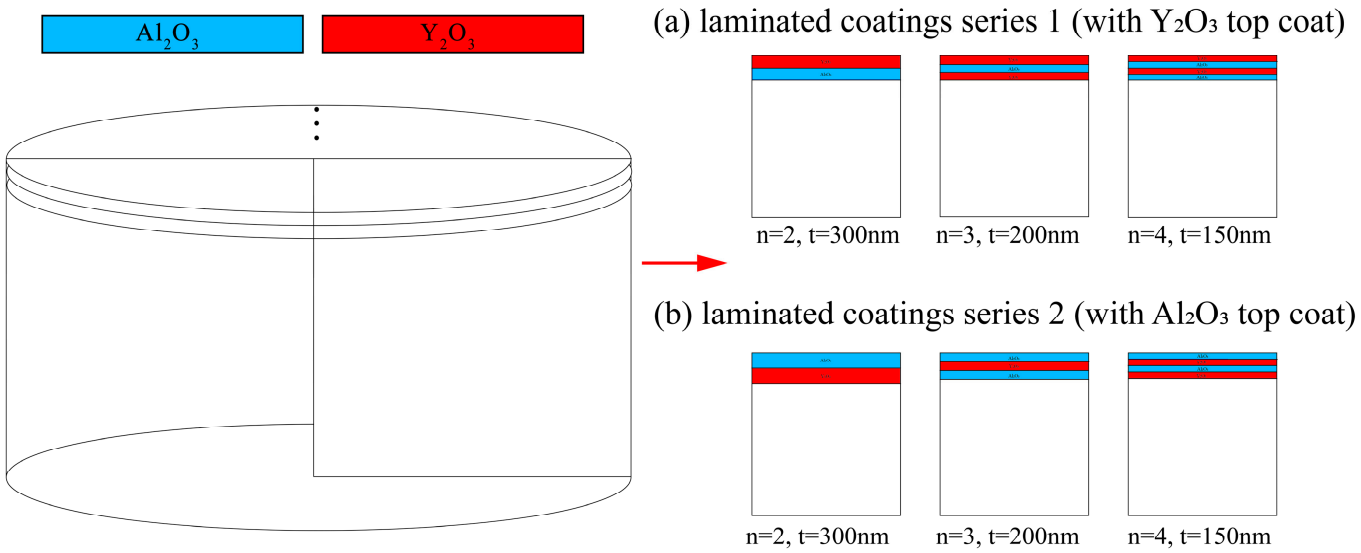

Figure 3. The geometry of the model: (**a**) laminated coating series 1 (with Y_2O_3 top coat); (**b**) laminated coating series 2 (with Al_2O_3 top coat).

Table 2. Model configuration.

Material	Density (kg/m^3)	Young's Modulus (GPa)	Poisson's Ratio	Coefficient of Thermal Expansion (CTE) (10^{-6} K^{-1})
316L	8000 [24]	200 [24]	0.25 [34]	17.3 [24]
am-Al_2O_3	3300 [35]	124.3 [36]	0.24 [36]	14.7 [37]
Y_2O_3	5000 [38]	120 [38]	0.26 [8]	8 [38]

2.3. Meshing

In order to build a nano-thick coating model with enough numerical scale for meshing, same methods applied in our previous study was used [33]. The micron was set as the standard unit of length in all models. Thus, all related parameters were converted to match the change (e.g., the Young's modulus of the Y_2O_3 is set to 0.12 N/μm^3). The elements in each layer are squares with 25 nm side length, while the element edge length of the substrate varies from 25 nm to 50 μm. Each model consists of approximately 500,000 elements and the average element quality is over 0.97. The mesh condition is shown in Figure 4.

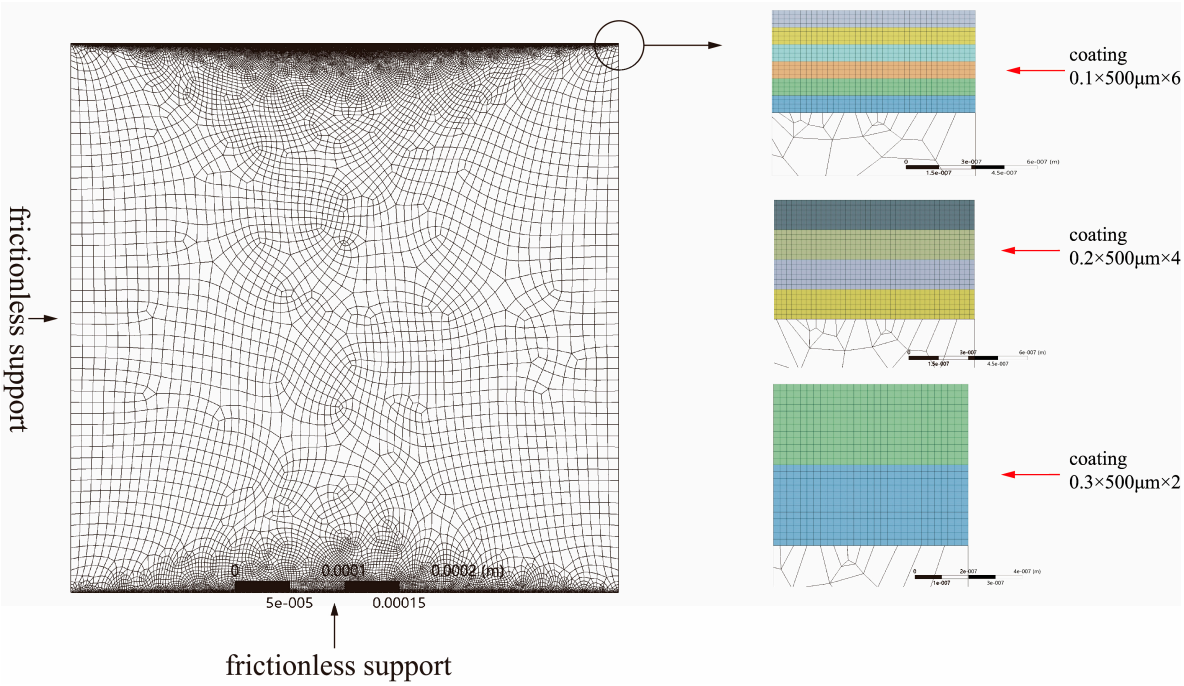

Figure 4. Mesh and boundary condition of the finite element.

2.4. Boundary Condition and Load

Frictionless supports were applied to the left edge and the bottom edge of the model, which prevented each edge from translating along its normal direction or rotating around itself. Bonded constraints were applied to each contact pair, causing the contacting surfaces to bond together. In other words, no relative tangential movements would occur on the interfaces. All models were cooled from a 700 °C stress-free state to a given terminal temperature, which simulated the condition of specimens in previous study; specimens annealed at 700 °C for stress relief purposes [32]. The boundary condition is shown in Figure 4.

3. Result and Discussion

3.1. Max Principal Stress in Laminated Coating with Different Layout, Number of Layers and Temperature

All laminated coatings were 600 nm thick, with the number of layers varying from two to four. The stress fields of each model were analyzed, and were also compared with the corresponding monolayer coatings with the same layer thickness. As shown in Figure 5, the max principal stress in the laminated coating series 1 (with Y_2O_3 top coat) increases as the layer thickness decreases, from 463 MPa for a two-layer coating to 495 MPa for a four-layer coating. While the max principal stress in the laminated coating series 2 (with Al_2O_3 top coat) decreases as the layer thickness decreases, from 657 MPa for a two-layer coating to 598 MPa for a four-layer coating. Moreover, the max principal stress in series 1 is about 25% lower than the series 2. The result shows that the laminated coating series 1 have better thermal cycle endurance than the series 2, which agrees to the previous experiment on bilayer coatings [32]. However, the max principal in both composite coatings is much higher than the monolayer coating with same layer thickness. The max principal stress in monolayer amorphous Al_2O_3 coating is only about 68 MPa, while the max principal stress in monolayer Y_2O_3 coating is about 230 MPa, which is much lower than that in the amorphous Al_2O_3 coating. The result reveals that the monolayer amorphous Al_2O_3 coating has better thermal cycle endurance than the monolayer Y_2O_3 coating, which agrees with the coefficient of thermal expansion (CTE) differences between the coating and the substrate in Table 2. The CTE of amorphous Al_2O_3 is 14.7×10^{-6} [37], while the CTE of Y_2O_3 is 8×10^{-6} [36], and the CTE of 316L SS is 17.3×10^{-6} [24]. The max principal stress

in both kinds of monolayer coating is almost even for the layer thickness from 150 nm to 300 nm. The thermal cycle endurances of monolayer amorphous Al_2O_3 and monolayer Y_2O_3 coating show little relevance to the coating thickness in the given condition of the simulation. Furthermore, the thermal stress of both kinds of laminated coatings is an order higher than that of the monolayer amorphous Al_2O_3 coating and about three times higher than that of the Y_2O_3 coating. The thermal mismatch between amorphous Al_2O_3 and Y_2O_3 is so large that becomes the major factor that determines the thermal residual stress in the coating system. It indicates that preparing this kind of laminated composite for better tritium permeation resistance comes at the cost of thermal cycle endurance.

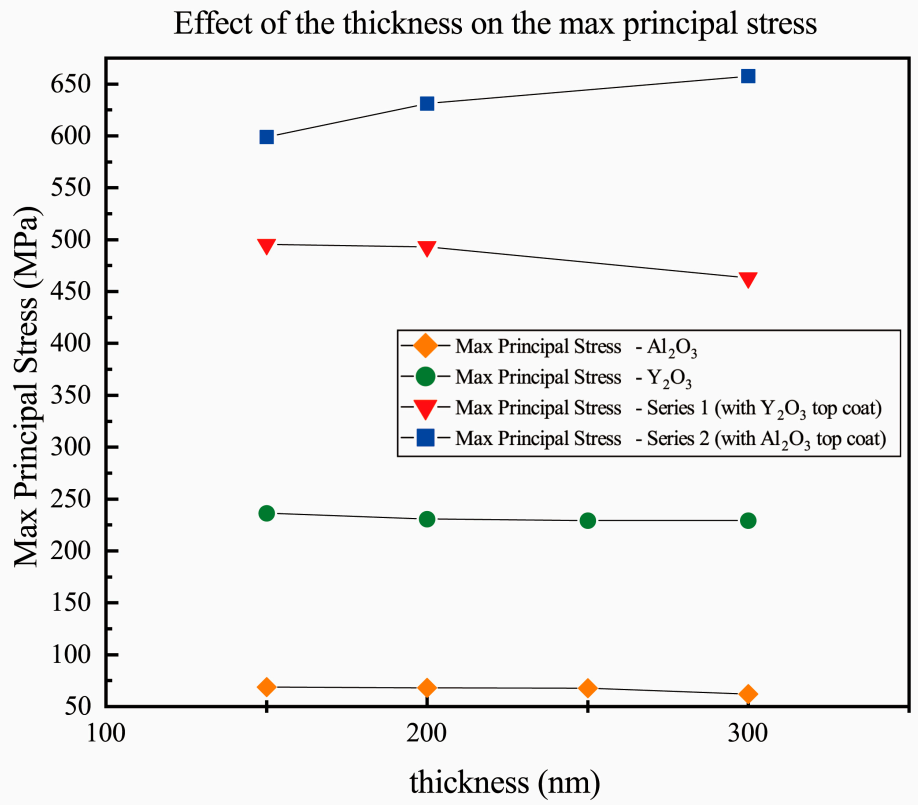

Figure 5. Effect of the thickness on the max principal stress of laminated coating and the corresponding monolayer coating.

As shown in Figure 6, the max principal stress in the laminated coating occurs in the layer adjacent to the top coat. The overall max principal stress in the layer beneath the top coat is the highest in all layers. The max principal stress distribution result agrees with the max stress data as shown in Figure 5, both showing that the thermal mismatch between the Y_2O_3 and amorphous Al_2O_3 is the major impact factor to the max principal stress in the coating system. The max principal stress site in bilayer Al_2O_3/Y_2O_3 coating is at the interface between the top coat and adjacent layer 25 nm from the edge. That in the bilayer Y_2O_3/Al_2O_3 coating is at the edge of the interface between the top coat and the adjacent layer 25 nm from the interface. On the other hand, the max principal stress site in three-layer and four-layer laminated coating locates inversely in the layers beneath the top coat compared with bilayer coating. The max principal stress sites in $Y_2O_3/Al_2O_3/Y_2O_3$ and $Al_2O_3/Y_2O_3/Al_2O_3/Y_2O_3$ coatings are at the interface between the sub-top layer and the adjacent layer beneath it 25 nm from the edge. The max principal stress sites in $Al_2O_3/Y_2O_3/Al_2O_3$ and $Y_2O_3/Al_2O_3/Y_2O_3/Al_2O_3$ coatings are at the edge of the sub-top layer 25 nm from the edge between the sub-top layer and the layer beneath. The result indicates that the sub-top layer is the most venerable in the Al_2O_3-Y_2O_3 laminated coating system with the most severe stress concentration. The surface of the sub-top layer is the

most likely crack initiation site that causes the final peeling-off of the laminated coating. It can be concluded that Y_2O_3 is not good to be directly composited with amorphous Al_2O_3 due to the vast thermal mismatch between them.

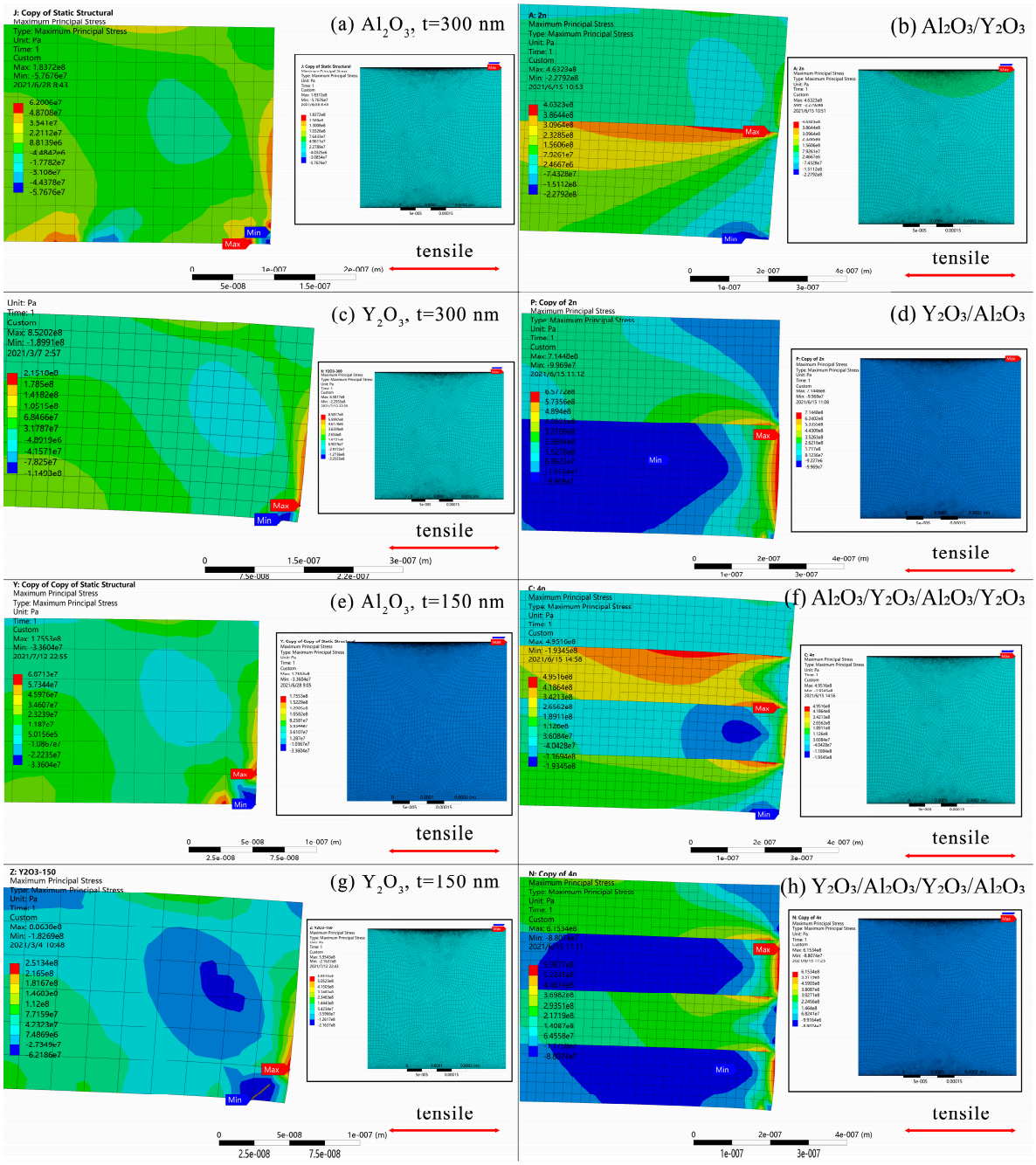

Figure 6. Comparison of the max principal stress in laminated coatings and single-layer coatings: (**a**) Al_2O_3, t = 300 nm; (**b**) Al_2O_3/Y_2O_3; (**c**) Y_2O_3, t = 300 nm; (**d**) Y_2O_3/Al_2O_3; (**e**) Al_2O_3, t = 150 nm; (**f**) $Al_2O_3/Y_2O_3/Al_2O_3/Y_2O_3$; (**g**) Y_2O_3, t = 150 nm; (**h**) $Y_2O_3/Al_2O_3/Y_2O_3/Al_2O_3$.

The decrease of max principal stress in the laminated coating series 2 (with Al_2O_3 top coat) as the layer thickness decreases can be explained by the stress singularity theory. At the edge of the interface, where there is a sudden change of stiffness, exists a stress singular

point. Furthermore, the residual thermal stress, σ_p, at the singular point can be express as follows when the singular region is small:

$$\sigma_p = \frac{K}{r^{\lambda}},\ r < r_0, \tag{9}$$

where r_0 is the vicinity zone of the stress singularity, and K is the stress intensity factor. Both K and λ are functions of the Poisson's ratio, Young's modulus, and the contact angles of the two layers. As the thickness of layers, t, increases, the λ decreases, the stress singularity zone becomes wider and the σ_p, at the edge increases. As a result, for laminated coating series 2 (with Al_2O_3 top coat), the more the layers, the thinner the layer, and the smaller the residual thermal stress will be [39]. However, as the number of layers increases, it can become increasingly difficult to deposit a laminated coating without critical defects. Furthermore, a less deformable layer could withstand stress with less deformation and have less impact to the coating system. In other words, there will be less stress singularity effect. Therefore, the max principal stress in laminated coating series 1 with more deformable top coat, Y_2O_3, and a less deformable sub-top coat Al_2O_3 withstanding the highest local stress in the coating system is lower than that in the series 2. An opposite effect, the increase in the max principal stress as the layer thickness increases, occurs due to the thinner Al_2O_3 layer to withstand the extra tensile stress caused by the strain of the adjacent less deformable Y_2O_3 layer.

The stress field of the model 3 (316L/Al_2O_3/Y_2O_3/Al_2O_3/Y_2O_3) cooling from a 700 °C stress-free state to different temperatures was simulated, with the result shown in Figure 7. It shows that the max principal stress declines linearly as the temperature difference decreases. This simulation result agrees with Equation (4) for thermal stress. However, if the crystallization and phase changes are taken into consideration, the actual result will be different from the simulation [40].

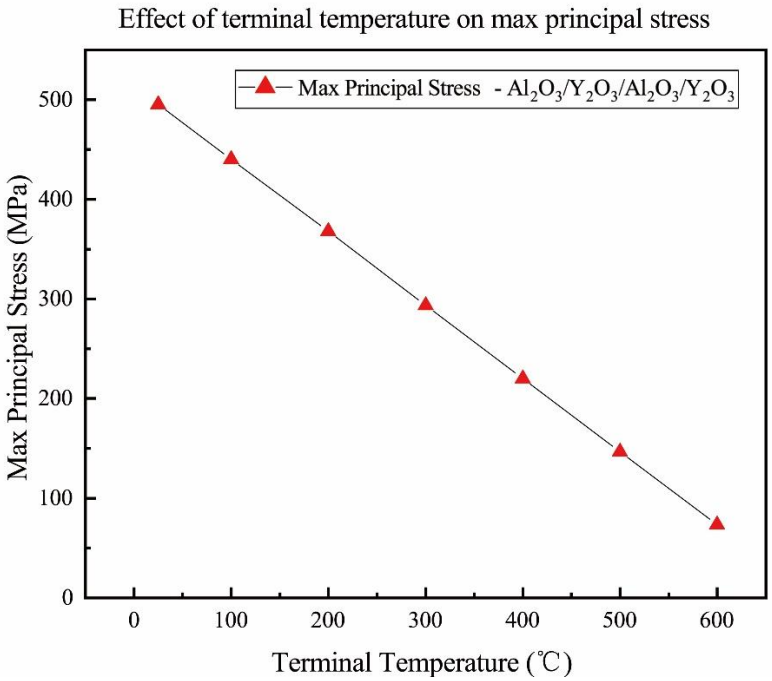

Figure 7. Effect of terminal temperature on the max principal stress.

3.2. Equivalent Elastic Strain and Neutral Plane in Laminated Coating

As shown in Figure 8, the equivalent elastic strain distribution shows that the neutral plane with nearly no strain is located at the horizontal center line of the substrate. This agrees with the theory proposed by Nix and colleagues [40]. However, the max elastic strain site in laminated coating series 1 is located near the center of the coating due to the

accumulating of strain while the max elastic strain site in laminated coating series 2 is located at the edge of the coating system. The more severe elastic strain in coating series 2 agrees with the stress analysis result that it endures greater stress. The result also shows that the contact surfaces have a great impact on the stress distribution as the elastic stress distribution differs to the max principal stress distribution.

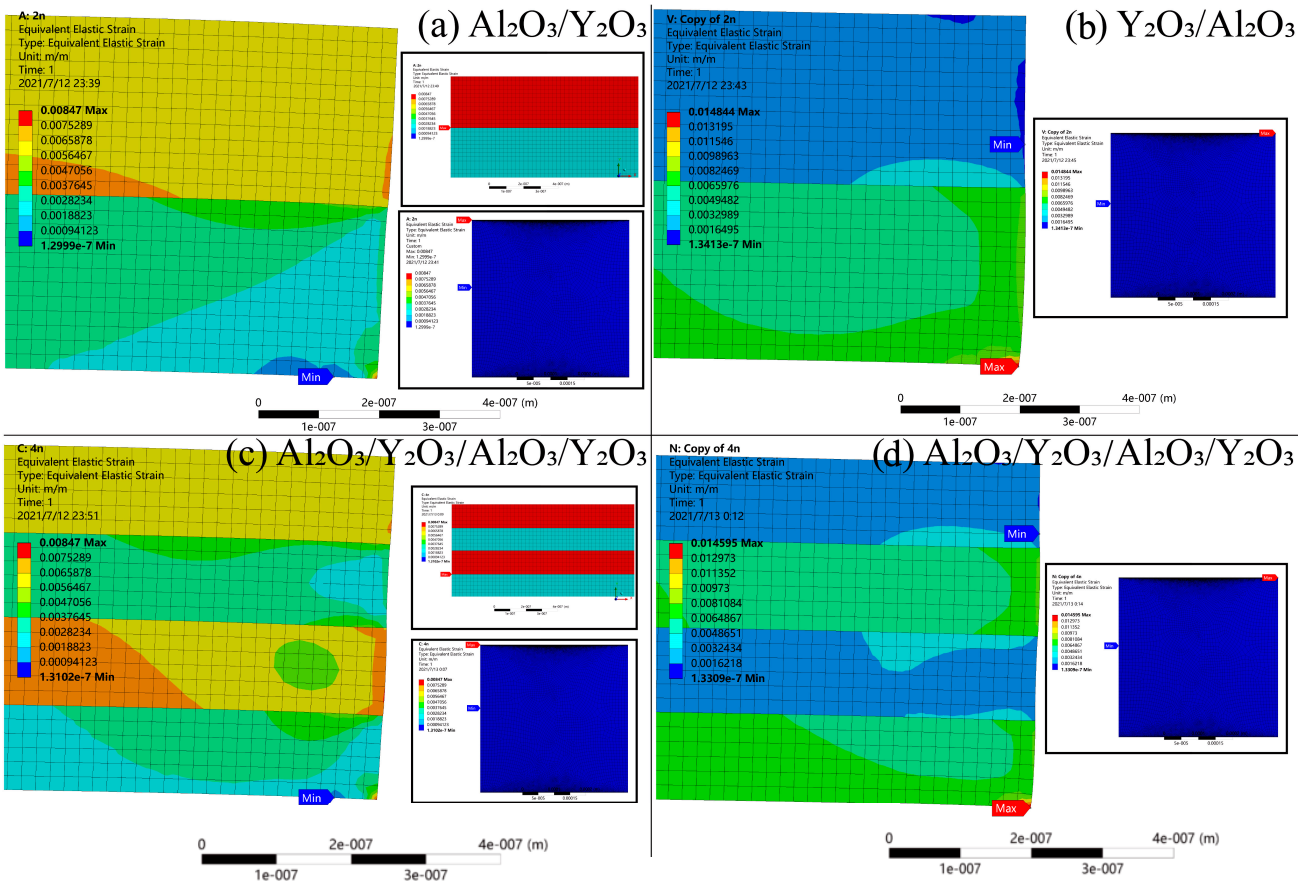

Figure 8. Equivalent elastic strain in laminated coatings: (**a**) Al_2O_3/Y_2O_3; (**b**) Y_2O_3/Al_2O_3; (**c**) $Al_2O_3/Y_2O_3/Al_2O_3/Y_2O_3$; (**d**) $Y_2O_3/Al_2O_3/Y_2O_3/Al_2O_3$.

The bending moment, M, for each layer can be determined by

$$M = -\left(\frac{E}{1-v}\right)\frac{t_s^3}{12}\kappa, \tag{10}$$

where E is the Young's modulus, v is the Poisson's ratio, $I = \frac{t_s^3}{12}$, is the moment of inertia for bending, and κ is the bending curvature.

By definition, the neutral plane fulfills the condition

$$M = 0 = \sum_{i=0}^{n} \int_{z_i}^{z_{i+1}} \varepsilon B_i (z-s) dz, \tag{11}$$

where $B = \left(\frac{E}{1-v}\right)$ is the biaxial modulus of the layers.

By matching the adjacent layers with the same amount of misfit strain, this leads to

$$s = \frac{1}{2}\frac{\sum_{i=0}^{n} B_i\left(z_{i+1}^2 - z_i^2\right)}{\sum_{i=0}^{n} B_i\left(z_{i+1} - z_i\right)}, \tag{12}$$

which for a bilayer coating leads to

$$s = \frac{1}{2}\frac{B_0 t_0^2 + B_1\left(t_1^2 + 2t_0 t_1\right)}{B_0 t_0 + B_1 t_1}. \tag{13}$$

As the substrate is much thicker and stiffer, $B_0 t_0 \gg B_1 t_1$, this relation can thus be simplified to $s = t_0/2$.

It can be derived that the curvature of the multiple-layer coating system is

$$\kappa = -\frac{\sum_{i-1}^{n} B_i \varepsilon_i^{misfit}\left\{\frac{1}{2}\left(z_{i+1}^2 - z_i^2\right) - s\left(z_{i+1} - z_i\right)\right\}}{\sum_{i=0}^{n} \frac{B_i}{3}\left\{\left(z_{i+1} - s\right)^3 - \left(z_i - s\right)^3\right\}}. \tag{14}$$

The result shows that the model proposed by Nix and his colleague [40] calculating the stress in multilayer system can predict the strain and stress in the system with acceptable accuracy.

4. Conclusions

In Al_2O_3-Y_2O_3 laminated coating, the amorphous Al_2O_3 layers with lower Young's modulus are more influential in the max principal stress in the thermal cycle behavior of the coating. The max principal stress in the laminated coating series 1, with a brittle Al_2O_3 sub-top layer withstanding the highest local stress in the system, increases as the layer thickness decreases. This is because, as the layer thickness decreases, the stress singularity zone at the edge of the interface decreases and its stress concentration effect increases. However, with a ductile Y_2O_3 sub-top layer (series 2), the max principal stress in the laminated coating increases as the layer thickness decreases. This is because the thinner the Y_2O_3 layers, the less stiffness they have to resist the extra tensile stress caused by the adjacent Al_2O_3 layer. The max principal stress in the laminated coating series 2 is about 25% higher than that in the laminated coating series 1 with the same layer thickness, meaning it is more prone to failure in dynamic thermal loadings. Thus, this kind of coating structures should be avoided. Both laminated coatings endure much greater stress than the monolayer coating, about three times higher than the monolayer Y_2O_3 coating and an order higher than the monolayer Al_2O_3 coating. The local stress concentrated most severely in the sub-top layer in laminated coating indicating the sub-top layer is the most likely position that the coating begins to fail into under thermal cycles. The residual thermal stress in the laminated coating declines linearly as the temperature difference declines, if the crystallization and phase changes are not taken into consideration. The neutral plane with no strain in the laminated coating is at the horizontal center line of the substrate.

Author Contributions: Conceptualization, Q.Y. and L.J.; methodology, K.H.; software, K.H.; validation, W.W., H.L.; formal analysis, K.H., B.Y.; investigation, H.L.; resources, W.X.; data curation, R.C.; writing—original draft preparation, K.H.; writing—review and editing, K.H., M.L.; visualization, H.L.; supervision, Y.L.; project administration, Q.Y. and L.H.; funding acquisition, J.M. All authors have read and agreed to the published version of the manuscript.

Funding: This research was funded by the Science Center for Gas Turbine Project (P2022-B-IV-009-002), the Opening Project fund of Materials Service Safety Assessment Facilities (MSAF series) and the Science and Technology Planning Project of Guangdong Province, China (2021B0909050001).

Institutional Review Board Statement: Not applicable.

Informed Consent Statement: Not applicable.

Data Availability Statement: Not applicable.

Conflicts of Interest: The authors declare no conflict of interest.

References

1. Wu, Y. Conceptual Design of the China Fusion Power Plant FDS-II. *Fusion Eng. Des.* **2008**, *83*, 1683–1689. [CrossRef]
2. Tanabe, T. *Tritium: Fuel of Fusion Reactors*; Springer: Tokyo, Japan, 2016. [CrossRef]
3. Fukada, S.; Oya, Y.; Hatano, Y. Review of Recent Japanese Activities on Tritium Accountability in Fusion Reactors. *Fusion Eng. Des.* **2016**, *113*, 231–235. [CrossRef]
4. Hanchar, D.R.; Kazimi, M.S. A Tritium Permeation Model for Conceptual Fusion Reactor Designs. *J. Fusion Energy* **1983**, *3*, 47–61. [CrossRef]
5. Annals of the ICRP. *Age-Dependent Doses to Members of the Public from Intake of Radionuclides: Part 4 Inhalation Dose Coefficients*; ICRP Publication 71; Ann. ICRP: Oxford, UK, 1995.
6. Smith, D.L.; Konys, J.; Muroga, T.; Evitkhin, V. Development of Coatings for Fusion Power Applications. *J. Nucl. Mater.* **2002**, *307–311*, 1314–1322. [CrossRef]
7. Huang, Q.; Li, C.; Wu, Q.; Liu, S.; Gao, S.; Guo, Z.; Yan, Z.; Huang, B.; Song, Y.; Zhu, Z.; et al. Progress in Development of CLAM Steel and Fabrication of Small TBM in China. *J. Nucl. Mater.* **2011**, *417*, 85–88. [CrossRef]
8. Otsuka, T.; Goto, K.; Yamamoto, A.; Hashizume, K. Effects of Shot-Peening on Permeation and Retention Behaviors of Hydrogen in Alpha Iron. *Fusion Eng. Des.* **2018**, *136*, 509–512. [CrossRef]
9. Yang, H.; Shao, Z.; Wang, W.; Ji, X.; Li, C. A Composite Coating of GO-Al_2O_3 for Tritium Permeation Barrier. *Fusion Eng. Des.* **2020**, *156*, 111689. [CrossRef]
10. Kulsartov, T.V.; Hayashi, K.; Nakamichi, M.; Afanasyev, S.E.; Shestakov, V.P.; Chikhray, Y.V.; Kenzhin, E.A.; Kolbaenkov, A.N. Investigation of Hydrogen Isotope Permeation through F82H Steel with and without a Ceramic Coating of Cr_2O_3-SiO_2 Including $CrPO_4$ (out-of-Pile Tests). *Fusion Eng. Des.* **2006**, *81*, 701–705. [CrossRef]
11. Houben, A.; Rasiński, M.; Gao, L.; Linsmeier, C. Tungsten Nitride as Tritium Permeation Barrier. *Nucl. Mater. Energy* **2020**, *24*, 100752. [CrossRef]
12. Wang, L.; Yang, J.J.; Feng, Y.J.; Li, F.Z.; Liao, J.L.; Yang, Y.Y.; Feng, K.M.; Liu, N. Preparation and Characterization of Al_2O_3 Coating by MOD Method on CLF-1 RAFM Steel. *J. Nucl. Mater.* **2017**, *487*, 280–287. [CrossRef]
13. Hu, L.; Wei, G.; Yin, R.; Hong, M.; Cheng, T.; Zhang, D.; Zhao, S.; Yang, B.; Zhang, G.; Cai, G.; et al. Significant Hydrogen Isotopes Permeation Resistance via Nitride Nano-Multilayer Coating. *Int. J. Hydrogen Energy* **2020**, *45*, 19583–19589. [CrossRef]
14. Averback, R.S.; Ehrhart, P.; Popov, A.I.; Sambeek, A.V. Defects in Ion Implanted And Electron Irradiated MgO and Al_2O_3. *Radiat. Eff. Defects Solids* **1995**, *136*, 169–173. [CrossRef]
15. Popov, A.I.; Lushchik, A.; Shablonin, E.; Vasil'chenko, E.; Kotomin, E.A.; Moskina, A.M.; Kuzovkov, V.N. Comparison of the F-type Center Thermal Annealing in Heavy-Ion and Neutron Irradiated Al_2O_3 Single Crystals. *Nucl. Instrum. Methods Phys. Res. Sect. B Beam Interact. Mater. At.* **2018**, *433*, 93–97. [CrossRef]
16. Li, H.; Ke, Z.; Xue, L.; Yan, Y. A Novel Low-Temperature Approach for Fabricating α-Al_2O_3-Based Ceramic Coating as Tritium Permeation Barrier. *Fusion Eng. Des.* **2017**, *125*, 567–572. [CrossRef]
17. Han, Q.; Geng, Y.; Setchi, R.; Lacan, F.; Gu, D.; Evans, S.L. Macro and Nanoscale Wear Behaviour of Al-Al_2O_3 Nanocomposites Fabricated by Selective Laser Melting. *Compos. Part B Eng.* **2017**, *127*, 26–35. [CrossRef]
18. Yang, F.; Xiang, X.; Lu, G.; Zhang, G.; Tang, T.; Shi, Y.; Wang, X. Tritium Permeation Characterization of Al_2O_3/FeAl Coatings as Tritium Permeation Barriers on 321 Type Stainless Steel Containers. *J. Nucl. Mater.* **2016**, *478*, 144–148. [CrossRef]
19. Huang, J.; Xie, H.; Luo, L.-M.; Zan, X.; Liu, D.-G.; Wu, Y.-C. Preparation and Properties of FeAl/Al_2O_3 Composite Tritium Permeation Barrier Coating on Surface of 316L Stainless Steel. *Surf. Coat. Technol.* **2020**, *383*, 125282. [CrossRef]
20. Liu, S.; Ju, X.; Qiu, J.; Chen, G.; Sun, J.; Xin, Y.; Ma, F. Tritium-Permeation-Barrier Properties of Erbium Oxide (TPB) Coating on CLAM Steel. *Fusion Eng. Des.* **2019**, *138*, 347–351. [CrossRef]
21. Xu, L.; Liu, S.; Wang, M.; Zhou, S. Crack Initiation and Propagation Mechanism of Al_2O_3-DBC Substrate during Thermal Cycling Test. *Eng. Fail. Anal.* **2020**, *116*, 104720. [CrossRef]
22. Liu, H.; Tao, J.; Gautreau, Y.; Zhang, P.; Xu, J. Simulation of Thermal Stresses in SiC-Al_2O_3 Composite Tritium Penetration Barrier by Finite-Element Analysis. *Mater. Des.* **2009**, *30*, 2785–2790. [CrossRef]
23. Liu, Z.; Meng, F.; Yi, L.B. Simulation of the Effects of Different Substrates, Temperature, and Substrate Roughness on the Mechanical Properties of Al_2O_3 Coating as Tritium Penetration Barrier. *Nucl. Sci. Tech.* **2019**, *30*, 62. [CrossRef]
24. Liu, H.; Tao, J.; Zhang, P.; Xu, J. Modeling of Residual Stresses in Functionally Gradient AI_2O_3 Coating on 316L Substrate. *J. Comput. Theor. Nanosci.* **2008**, *5*, 1677–1680. [CrossRef]
25. Stylianou, R.; Velic, D.; Daves, W.; Ecker, W.; Tkadletz, M.; Schalk, N.; Czettl, C.; Mitterer, C. Thermal Crack Formation in TiCN/α-Al_2O_3 Bilayer Coatings Grown by Thermal CVD on WC-Co Substrates with Varied Co Content. *Surf. Coat. Technol.* **2020**, *392*, 125687. [CrossRef]
26. de la Roche, J.; Gómez, P.A.; Alvarado-Orozco, J.M.; Toro, A. Hot Corrosion and Thermal Shock Resistance of Dense-CYSZ/YSZ Bilayer Thermal Barrier Coatings Systems Applied onto Ni-Base Superalloy. *J. Eur. Ceram. Soc.* **2020**, *40*, 5692–5703. [CrossRef]
27. Li, B.; Fan, X.; Wang, T.; Zhou, K. Interfacial Fracture Behavior of Double-Ceramic-Layer Thermal Barrier Coating System with Segmented Structure. *Eng. Fract. Mech.* **2018**, *201*, 13–28. [CrossRef]
28. Rezaei, S.; Wulfinghoff, S.; Reese, S. Prediction of Fracture and Damage in Micro/Nano Coating Systems Using Cohesive Zone Elements. *Int. J. Solids Struct.* **2017**, *121*, 62–74. [CrossRef]

29. Li, B.; Fan, X.; Okada, H.; Wang, T. Mechanisms Governing the Failure Modes of Dense Vertically Cracked Thermal Barrier Coatings. *Eng. Fract. Mech.* **2018**, *189*, 451–480. [CrossRef]
30. Seo, S.B.; Bang, I.C. Effects of Al_2O_3 Nanoparticles Deposition on Critical Heat Flux of R-123 in Flow Boiling Heat Transfer. *Nucl. Eng. Technol.* **2015**, *47*, 398–406. [CrossRef]
31. Zhou, C.; Wang, N.; Xu, H. Comparison of Thermal Cycling Behavior of Plasma-Sprayed Nanostructured and Traditional Thermal Barrier Coatings. *Mater. Sci. Eng. A* **2007**, *452–453*, 569–574. [CrossRef]
32. Wang, W.; Yu, Q.; Liu, X.; Lu, Z. Preparation of Al_2O_3/Y_2O_3 Composite Coating for Deuterium Permeation Reduction. *J. Rare Earths* **2020**, *38*, 1237–1242. [CrossRef]
33. Huang, K.; Wang, W.; Yu, Q.; Hao, L.; Mi, J.; Li, S.; Liu, H.; Li, S.; Liu, J.; Wang, J. Simulation of the Residual Stress of the Y_2O_3/Al_2O_3 Composite Deuterium Permeation Barrier under Thermal Shock. *Int. J. Photoenergy* **2021**, *2021*, 6684802. [CrossRef]
34. Konynenburg, R.A.; McCright, R.D.; Roy, A.K.; Jones, D.A. *Engineered Materials Characterization Report for the Yucca Mountain Site Characterization Project Volume 2: Design Data*; Lawrence Livermore National Lab: Livermore, CA, USA, 1995.
35. Shi, C.; Alderman, O.L.G.; Berman, D.; Du, J.; Neuefeind, J.; Tamalonis, A.; Weber, J.K.R.; You, J.; Benmore, C.J. The Structure of Amorphous and Deeply Supercooled Liquid Alumina. *Front. Mater.* **2019**, *6*, 38. [CrossRef]
36. Rontu, V.; Nolvi, A.; Hokkanen, A.; Haeggström, E.; Kassamakov, I.; Franssila, S. Elastic and Fracture Properties of Free-Standing Amorphous ALD Al_2O_3 Thin Films Measured with Bulge Test. *Mater. Res. Express* **2018**, *5*, 046411. [CrossRef]
37. Huntz, A.-M.; Andrieux, M.; Vahlas, C.; Sovar, M.-M.; Samelor, D.; Gleizes, A.N. Phase Transformations of Metallorganic Chemical Vapor Deposition Processed Alumina Coatings Investigated by In Situ Deflection. *J. Electrochem. Soc.* **2007**, *154*, 63. [CrossRef]
38. Martienssen, W.; Warlimont, H. *Springer Handbook of Condensed Matter and Materials Data*; Springer: Berlin/Heidelberg, Germany, 2005.
39. Gu, B.; Phelan, P.E. Thermal Peeling Stress Analysis of Thin-Film High-Tc Superconductors. *Appl. Supercond.* **1998**, *6*, 19–29. [CrossRef]
40. Nix, W.D. Metallic Thin Films: Stresses and Mechanical Properties. In *Metallic Films for Electronic, Optical and Magnetic Applications: Structure, Processing and Properties*; Woodhead Publishing: Cambridge, UK, 2013; pp. 353–421. [CrossRef]